EDGE ARTICLE

Check for updates

All publication charges for this article have been paid for by the Royal Society of Chemistry

High-efficiency blue thermally activated delayed fluorescence from donor–acceptor–donor systems *via* the through-space conjugation effect†

Feifei Gao,‡ Ruiming Du,‡ Chunmiao Han, Jing Zhang, Ying Wei, Guang Lu and Hui Xu [ID] *

The photophysical optimization of donor (D)–acceptor (A) molecules is a real challenge because of the intrinsic limitation of their charger transfer (CT) excited states. Herein, two D–A–D molecules featuring blue thermally activated delayed fluorescence (TADF) are developed, in which a homoconjugated acceptor 5,10-diphenyl-5,10-dihydrophosphanthrene oxide (DPDPO2A) is incorporated to bridge four carbazolyl or 3,6-di-*t*-butyl-carbazolyl groups for D–A interaction optimization without immoderate conjugation extension. It is shown that the through-space conjugation effect of DPDPO2A can efficiently enhance intramolecular CT (ICT) and simultaneously facilitate the uniform dispersion of the frontier molecular orbitals (FMO), which remarkably reduces the singlet–triplet splitting energy (ΔE_{ST}) and increases FMO overlaps for radiation facilitation, resulting in the 4–6 fold increased rate constants of reverse intersystem crossing (RISC) and singlet radiation. The maximum external quantum efficiency beyond 20% and the state-of-the-art efficiency stability from sky-blue TADF OLEDs demonstrate the effectiveness of the "conjugation modulation" strategy for developing high-performance optoelectronic D–A systems.

1. Introduction

Organic donor–acceptor (D–A) molecules feature charge-transfer (CT) excited states and ambipolar characteristics,[1,2] and therefore are widely used in optoelectronic applications, such as organic light-emitting diodes (OLEDs),[3–25] organic solar cells (OSCs),[26–34] photodetectors,[35,36] memory devices,[37–39] and so on.[40–44] The electrical properties of D–A systems are readily modulated on the basis of the inherent relationship between molecules and D/A groups regarding electron gain and loss.[45] In contrast, the photophysical properties of D–A molecules are more difficult to optimize due to the strong dependence of the excited-state characteristics on the intramolecular CT (ICT) interaction.[46] For instance, thermally activated delayed fluorescence (TADF) materials emerge recently for OLED applications, which should have near-zero singlet–triplet splitting energy (ΔE_{ST}) to facilitate reverse intersystem crossing (RISC)

Key Laboratory of Functional Inorganic Material Chemistry, Ministry of Education & School of Chemistry and Material Science, Heilongjiang University, 74 Xuefu Road, Harbin 150080, People's Republic of China. E-mail: hxu@hlju.edu.cn; ywei@hlju.edu.cn

for delayed fluorescence (DF).[47–51] It is known that ΔE_{ST} is twice the electron exchange energy (J) expressed as:[52,53]

$$\Delta E_{ST} = 2J = 2 \iint \Psi_L(1)\Psi_H(2)\left(\frac{e^2}{r_1 - r_2}\right)\Psi_L(2)\Psi_H(1)\mathrm{d}r_1\mathrm{d}r_2 \quad (1)$$

where Ψ_H and Ψ_L refer to the wave functions of the highest occupied and the lowest unoccupied molecular orbitals (HOMO and LUMO), respectively. On the other hand, according to Fermi's golden rule,[54] the transition probability (Γ) between the initial and final states can be described as:

$$\Gamma = \frac{2\pi}{h}\rho\langle H\rangle^2 \quad (2)$$

$$\langle H\rangle = \langle \Psi_I|\mu|\Psi_F\rangle = \int \Psi_I er\Psi_F \mathrm{d}\tau \quad (3)$$

where ρ is the density of final states, $\langle H\rangle$ is the matrix element for the interaction, and Ψ_I and Ψ_F refer to the wave functions of the initial and final states, respectively. μ, e and r are the transition dipole moment operator, electron charge and electron transition distance, respectively. On account of the CT singlet excited states (^{1}CT) for TADF molecules, their ΔE_{ST} and Γ are simultaneously in direct proportion to the HOMO–LUMO overlap integral $\langle \Psi_H|\Psi_L\rangle$, making the achievement of efficient DF become a real challenge.

Obviously, the conflict between ΔE_{ST} and Γ could be resolved by finding the best compromise for $\langle \Psi_H|\Psi_L\rangle$.[10,55] Although it

was shown that the moderate HOMO–LUMO overlap is an essential condition for improving the radiative efficiency of TADF molecules, the optimal frontier molecular orbital (FMO) distribution is still ambiguous, which limits the targeted molecular design. From another perspective, Adachi *et al.* demonstrated that the delocalization of the HOMO and the LUMO can enhance the radiative rate of CT compounds through increasing the oscillator strength of their ^{1}CT radiation despite small $\langle \Psi_H | \Psi_L \rangle$, which can be realized through either dendronizing the D group[56] or increasing the density of D groups linked on the same π-bridge.[10] The former more or less increases the synthesis complexity, whereas the latter leads to a remarkable bathochromic shift of the emission. Actually, because of the high sensitivity of emission color to the intensity of D–A interactions, the excited-state characteristics of blue TADF materials are even more difficult to modify.[57,58]

As alternatives, D–A–D and D–A–A type molecules seem promising, owing to their advantage of accurate ICT modulation.[59,60] The D–A–D structure could be regarded as the combination of two D–A units with doubled but dispersed D and A groups. Lee *et al.* constructed a D–A–D dye through the single-bond linkage of two isophthalonitrile acceptors, which resulted in the LUMO delocalization, 1.5-fold photoluminescence quantum yield (PLQY, ϕ_{PL}) and twofold external quantum efficiency (EQE, η_{EQE}) of its devices, however, accompanied by a remarkable emission red shift (~50 nm).[61] In contrast, through incorporating P=O as the insulating acceptor, we realized a pure-blue D–A–D TADF dye, but its HOMO and LUMO were still localized on single D/A groups.[62] Obviously, the conjugation between D–A units should be precisely modulated to optimize electronic interplays.[63] In this sense, systems based on homoconjugation would be the desired alternatives, whose through-space conjugation effect on intramolecular electronic communications is between the through-bond conjugation and insulating effects.[64] Therefore, they could not only support sufficient D–A interactions, but also avert immoderate conjugation extension, and are "ideal" for developing high-efficiency blue TADF dyes (Scheme 1).

It is noteworthy that the lengths of homoconjugated units are commonly larger than diphenylene, which would weaken D–A interactions, if used as π-linkers.[65] In such a case, a homoconjugated acceptor is desired, since it can directly combine with D groups to provide strong enough ICT effects and simultaneously suppress excessive intramolecular electronic interactions. As a proof of concept, in this contribution, we incorporate a homoconjugated phosphine oxide (PO) acceptor 5,10-diphenyl-5,10-dihydrophosphanthrene oxide (DPDPO2A) into D–A–D systems 9,9′,9″,9‴-(5,10-diphenyl-5,10-dihydrophosphanthrene-2,3,7,8-tetrayl)tetrakis(9H-carbazole) oxides (**4CzDPDPO2A**) and 9,9′,9″,9‴-(5,10-diphenyl-5,10-dihydrophosphanthrene-2,3,7,8-tetrayl)tetrakis(3,6-di-*tert*-butyl-9H-carbazole) oxides (**4tBCzDPDPO2A**), collectively named **4ArDPDPO2A** (Ar = Cz or tBCz), in which carbazoles (Cz) and 3,6-di-*tert*-butyl-carbazoles (tBCz) serve as D groups, respectively (Fig. 1a). In contrast to their insulated congeners **4ArPPOPO** and **4ArPPODPO** with completely localized HOMOs and LUMOs, the homoconjugated DPDPO2A acceptor dramatically facilitates intramolecular
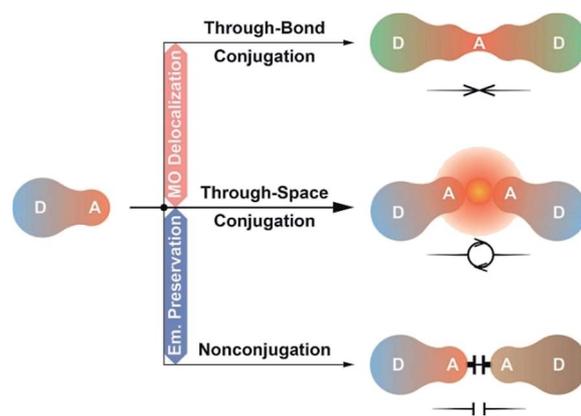
Scheme 1 Molecular design of D–A–D systems. Two D–A type molecules can be combined to form (i) a uniform D–A–D system based on through-bond conjugation, (ii) a united D–A–D system based on through-space conjugation or (iii) a separated D–A–A–D system based on insulating linkage.

electronic interplays, providing HOMOs and LUMOs uniformly dispersed on D and A groups, respectively, which shortens the centroid distances and increases the overlap integrals between the HOMOs and the LUMOs, accompanied by enhanced ICT effects. As a result, the doped films of **4CzDPDPO2A** and **4tBCzDPDPO2A** reveal pure-blue and sky-blue emissions with 4–6 fold increased rate constants of prompt fluorescence (PF, k_{PF}) and singlet radiation (k_r^S) and 2–4 fold increased DF rate constants (k_{DF}), as well as dramatically improved RISC efficiencies (ϕ_{RISC}) of 85 and 94%, respectively. As expected, **4CzDPDPO2A** and **4tBCzDPDPO2A** achieve photoluminescence (PL, ϕ_{PL}) and electroluminescence (EL, η_{EQE}) quantum efficiencies of 65 and 81% and 11.5 and 23.7%, respectively, which are 2–10 times higher in comparison to **4ArPPOPO** and **4ArPPODPO**, making them favorable among the blue TADF dyes reported to date. This work demonstrates a facile strategy to optimize the electronic effect in D–A molecules through conjugation modulation, which provides a new way to overcome the bottlenecks of their optoelectronic applications.

2.   Results and discussion

2.1.   Design and structures

We choose our previously reported blue TADF molecules **o2ArPO** as the D–A unit, whose simple D–π–A structures consist of Cz/tBCz and diphenylphosphine oxide (DPPO) as D and A groups, respectively.[66] Although their HOMOs are uniformly dispersed on the Cz/tBCz groups, their LUMOs are localized on the single phenyls. Despite the pure-blue emissions, the limited D–A interactions result in relatively low ϕ_{PL} and η_{EQE} less than 50 and 10%, respectively, for **o2ArPO**. From the D–π–A structures of **o2ArPO** to the D–A–D structures, when two P=O groups are used to simultaneously link two Cz/tBCz substituted phenyls at *ortho* positions, the cyclic DPDPO2A acceptor with the feature of through-space conjugation and the homoconjugated **4ArDPDPO2A** are formed; when the single P=O group is used as an insulating linkage between two D–A units, **4ArPPOPO** and
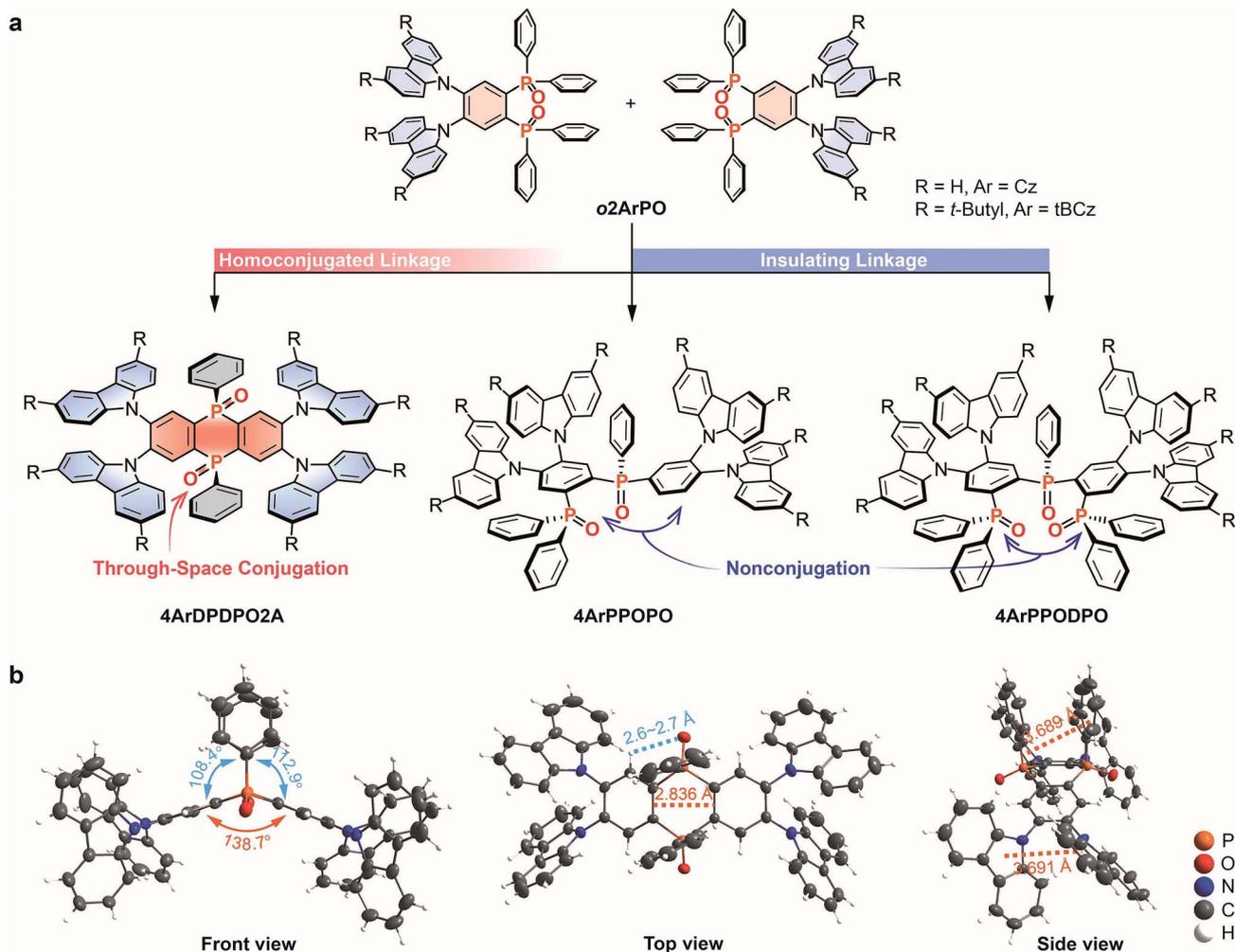
Fig. 1 Design and structure of **4ArDPDPO2A**, **4ArPPOPO** and **4ArPPODPO**. (a) Molecular design of **4ArDPDPO2A**, **4ArPPOPO** and **4ArPPODPO** as the dimers of *o2ArP2PO* on the basis of homoconjugated and insulating linkages, respectively; (b) Front, top and side views of the single-crystal structure for **4CzDPDPO2A**.

4ArPPODPO with nonconjugated D–A–D structures are formed. The D/A ratios in **4ArPPOPO** and **4ArDPDPO2A** are equal, but the D–A interaction intensity in each D–A unit of **4ArPPODPO** is comparable to that in **4ArDPDPO2A** (Scheme S1†). Actually, the basic structure of these molecules is the same as that of a P=O-based acceptor substituted with four carbazole-based donors (Scheme S2†). In this case, the only structural difference between **4ArDPDPO2A**, **4ArPPOPO** and **4ArPPODPO** is the conjugation extent, which should be the main reason leading to their diverse photophysical properties.

The single-crystal structure of **4CzDPDPO2A** indicates a nearly coplanar DPDPO2A ring with a large dihedral angle of ∼140°, which should be ascribed to the strong intramolecular hydrogen bonds between P=O groups and H atoms at both-side *ortho* positions with H···O distances less than 3 Å (Fig. 1b). The intramolecular hydrogen bonds also give rise to the *cis* configuration of DPDPO2A with coplanar P=O groups, in which two same-side phenyls reveal the intramolecular π–π interaction with a centroid–centroid distance of ∼3.8 Å. Similarly, the *ortho*-substitution enables intramolecular π–π interactions between

adjacent Cz groups with a centroid–centroid distance of ∼3.7 Å. More importantly, the distance between two C=C bonds in the 1,4-diphosphinine oxide unit is 2.84 Å, which is short enough for the p-orbital overlap.[67] These intramolecular interplays not only result in the planar phosphanthrene ring with potential homoconjugation, but also enhance the molecular rigidity to increase ϕ_{PL}.[59] In the packing diagram, **4CzDPDPO2A** reveals two different orientations, which are alternately aligned along the axis (Fig. S1†). The centroid-to-edge distance between Cz and DPDPO2A groups in adjacent molecules within 3.7 Å indicates a weak intermolecular charge transfer interaction, which in turn evidences the predominant influence of ICT effect on photophysical properties.

Although the crystals of **4tBCzDPDPO2A** cannot be obtained, on account of the negligible intramolecular steric hindrance for 3,6-*tert*-butyls of the peripheral tBCz groups, the configurations of **4ArDPDPO2A** would be similar, which is further demonstrated by the density functional theory (DFT) simulation (Fig. S2–S4†). In contrast, due to the C–P bond rotation of their P=O linkers, the structures of **4ArPPOPO** and **4ArPPODPO** are

more flexible, twisted and asymmetrical, which not only induces differences between two D–A units in spatial orientation, but also suppresses intermolecular interactions.[21,68] As a result, the thermal stability of **4ArDPDPO2A** is remarkably higher than that of **4ArPPOPO** and **4ArPPODPO**, but all the materials reveal a stable amorphous phase in the solid state (Fig. S5†). Because **4ArDPDPO2A**, **4ArPPOPO** and **4ArPPODPO** are comparable regarding intermolecular interactions, it is rational to attribute their optical properties to their single molecule characteristics.

2.2. DFT and TDDFT simulations

DFT and time-dependent DFT (TDDFT) calculations were performed to figure out the frontier molecular orbital (FMO) distributions and the excitation characteristics. As depicted in Fig. 2a, the HOMOs of **4ArDPDPO2A** are almost equally dispersed on their four Cz/tBCz groups, accompanied by minor

contributions from phosphanthrene rings. Their HOMO+1s and HOMO+2s also reveal similar distributions (Fig. S2 and S3†). Meanwhile, the LUMOs, LUMO+1s and LUMO+2s of **4ArDPDPO2A** are uniformly dispersed on their DPDPO2A groups. It should be noticed that for the LUMOs and LUMO+1s, the electronic wave functions of p-orbitals of sp^2-hybrid C atoms at two sides of P atoms are effectively and directly overlapped without the incorporation of orbitals from P atoms, convincingly evidencing through-space conjugation between the "P=O-separated" phenylenes in phosphanthrene rings (Fig. S4†). In contrast, the HOMOs and LUMOs of **4ArPPOPO** and **4ArPPODPO** are basically localized at one-to-two Cz/tBCz groups on one side of the molecules and the phenyls linked with P=O groups. Furthermore, FMOs of **4ArPPODPO** are more centralized than those of **4ArPPOPO**, due to the stronger D–A interactions in the former. Therefore, as expected, in contrast to insulating linkage, the homoconjugated acceptors in D–A–D molecules can dramatically facilitate FMO delocalization,
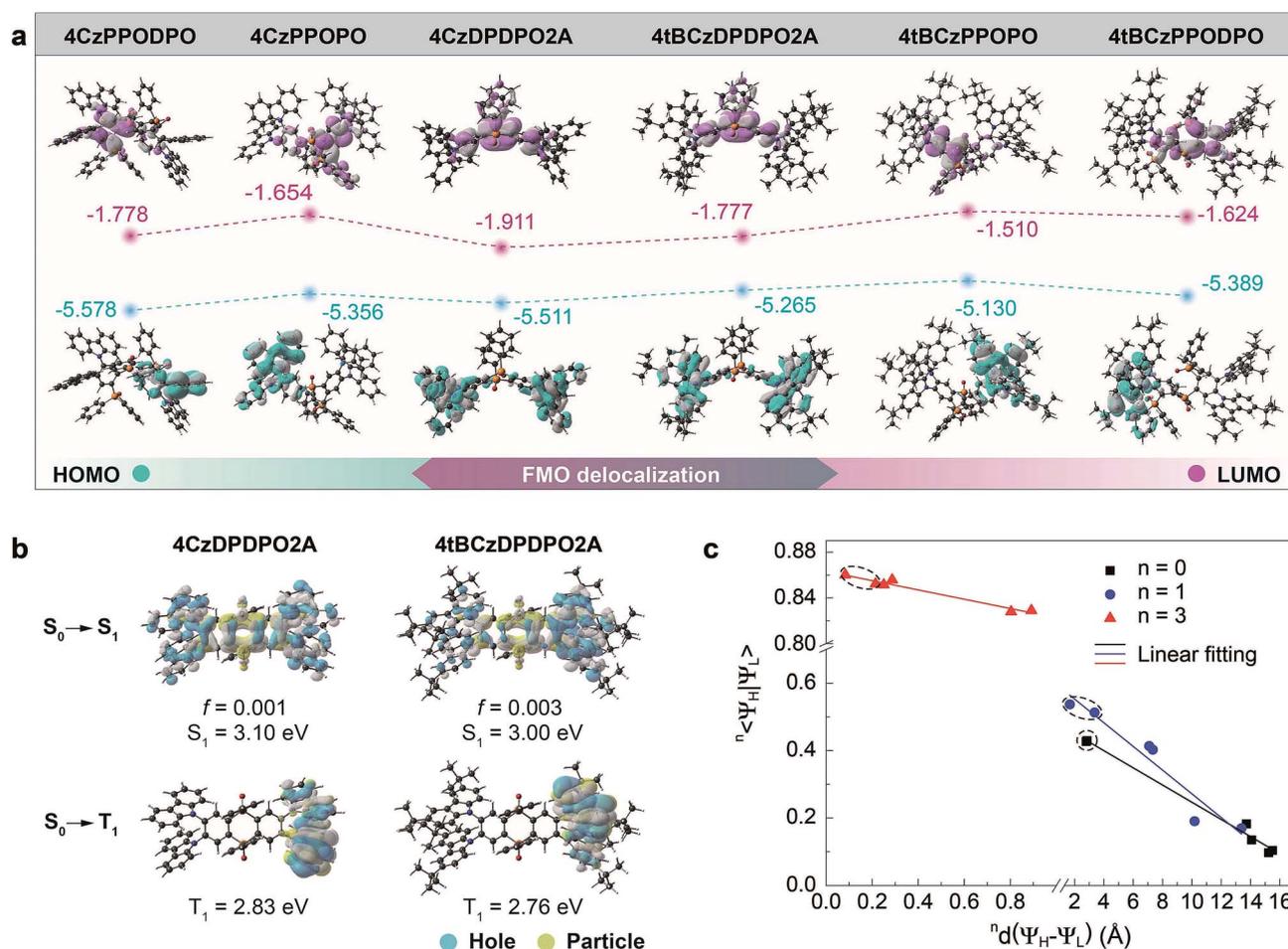

Fig. 2 Theoretical simulation of **4ArDPDPO2A**, **4ArPPOPO** and **4ArPPODPO**. (a) Contours and energy levels of the HOMOs and LUMOs for the S_0 states of **4ArDPDPO2A**, **4ArPPOPO** and **4ArPPODPO** simulated with the DFT method (B3LYP/6-31g*); (b) contours of the "hole" and "particle" and the constants of the singlet and triplet excitations for **4ArDPDPO2A** simulated with the TDDFT method (ωB97XD/6-31g*). S_1 and T_1 refer to the first singlet and triplet energy levels. f is the oscillator strength of $S_0 \rightarrow S_1$ excitation. For comparison, the NTO results of **4ArPPOPO** and **4ArPPODPO** are shown in Fig. S4;† (c) correlations between the centroid distance ($^nd(\Psi_H - \Psi_L)$) and overlap integral ($^n\langle\Psi_H|\Psi_L\rangle$) of the frontier orbitals for the S_0, S_1 and T_1 states of **4ArDPDPO2A**, **4ArPPOPO** and **4ArPPODPO**. The values 0, 1 and 3 of superscript n refer to the S_0, S_1 and T_1 states, respectively. The data of **4ArDPDPO2A** are distinguished with dashed circles.

especially leading to uniform HOMO dispersion on all D groups at both sides of the acceptors.

The HOMO energy levels of the compounds are basically in accord with their D groups whose HOMO values are equal to ~-5.4 eV for Cz and ~-5.2 eV for tBCz (Fig. 2a, S2, S3 and Table S1†). Differently, the LUMOs of **4ArDPDPO2A** are remarkably deeper than those of **4ArPPOPO** and **4ArPPODPO** by 0.15 and 0.25 eV, respectively, which reflects the stronger electron-withdrawing effect of the DPDPO2A group. Furthermore, it is noteworthy that the HOMO–LUMO energy gaps of **4ArDPDPO2A** are 0.1 and 0.2 eV smaller than those of **4ArPPOPO** and **4ArP-PODPO**, respectively, which is perfectly consistent with the results of cyclic voltammetry (CV) analysis (Fig. S6 and Table S2†). The measured HOMO energy levels of **4ArDPDPO2A** are about 0.05 eV smaller than those of their analogues, while the HOMO energy levels of **4ArPPOPO** and **4ArPPODPO** are equivalent. Therefore, in comparison to **4ArPPOPO**, the doubled DPPO groups at both sides of **4ArPPODPO** can hardly influence the HOMOs contributed by the D groups, which further manifests their localized ICT interactions only contributed by single D–A units. In opposite, the experimental values of the LUMO energy levels for **4ArDPDPO2A**, **4ArPPOPO** and **4ArPPODPO** gradually decrease from ~3.3, ~3.1 to ~3.0 eV. It is rational that the larger steric hindrance of two *ortho*-DPPO groups in **4ArP-PODPO** provides a more twisted configuration and further reduces the ICT effect, leading to their highest LUMO energy levels. Besides the stronger electron-withdrawing effect of DPDPO2A acceptors, the deepest LUMOs and HOMOs of **4ArDPDPO2A** should be actually attributed to the strongest ICT interactions between their DPDPO2A and Cz/tBCz groups. This is further evidenced by their smallest experimental HOMO–LUMO energy gaps of ~2.8 eV, which is as much as 0.2 and 0.3 eV smaller than those of **4ArPPOPO** and **4ArPPODPO**, respectively. Consequently, the incorporation of homo-conjugated DPDPO2A as the acceptor can indeed improve the ICT effect, owing to its through-space conjugation effect facilitated D–A interactions.

Natural transition orbital (NTO) analysis of singlet and triplet excitations was performed to identify the excited-state characteristics (Fig. 2b and S7†).[69,70] For $S_0 \rightarrow S_1$ excitations of **4ArDPDPO2A**, similar to the FMO locations of their ground states (S_0), the "holes" are uniformly dispersed on their four D groups, accompanied by minor contributions from phenylenes of DPDPO2A rings, while the "particles" are mainly distributed on their DPDPO2A groups, manifesting their CT-predominant first singlet excited states (S_1). In contrast, the S_1 states of **4ArPPOPO** and **4ArPPODPO** are completely localized with the "holes" on single D groups and the "particles" on single phenylenes linked with P=O groups. The significantly delocalized S_1 states of **4ArDPDPO2A** undoubtedly originate from the through-space conjugation effect of DPDPO2A for the uniformity of D–A interactions in whole molecules. The insulating P=O linkages in **4ArPPOPO** and **4ArPPODPO** in turn impede the electronic communications between two D–A units, resulting in their locally confined S_1 states. It is noteworthy that comparable to their insulated analogues, the S_1 energy levels of **4ArDPDPO2A** (~3.0 eV) are only slightly lower by 0.1 eV, still

corresponding to blue emissions, which manifests the limited influence of the homoconjugated linkage on emission color. On the other hand, for $S_0 \rightarrow T_1$ excitations, all the molecules reveal LE T_1 states with the "holes" and "particles" localized on their Cz groups, which benefits the RISC transitions from the T_1 to the S_1.[71] Although the planar geometry of the DPDPO2A acceptor is a requirement, its homoconjugation is the main reason for the preserved excited-state energy levels and enhanced ICT effect of **4ArDPDPO2A**.

The overlap integrals ($^n\langle \Psi_H | \Psi_L \rangle$) and the centroid distances ($^nd(\Psi_H - \Psi_L)$) of the FMOs for the S_0, S_1 and T_1 states, respectively corresponding to $n = 0$, 1 and 3, are estimated to quantitatively investigate the influence of conjugation on orbital distribution (Fig. 2c and Table S1†).[72] In accordance with their LE T_1 states, all the molecules have comparable $^3\langle \Psi_H | \Psi_L \rangle$ as large as 0.8, accompanied by negligible $^3d(\Psi_H - \Psi_L)$. However, $^0\langle \Psi_H | \Psi_L \rangle$ values of **4ArDPDPO2A** reach 0.43, which is 2 and 4 fold those of **4ArPPOPO** and **4ArPPODPO**. Especially, $^0d(\Psi_H - \Psi_L)$ values of **4ArDPDPO2A** are extremely small and are equal to 2.8 Å, which is extraordinary for D–A systems and only one seventh of those of **4ArPPOPO** and **4ArPPODPO**. Such small $^0d(\Psi_H - \Psi_L)$ values undoubtedly benefit from the uniformly and symmetrically dispersed HOMOs and LUMOs of **4ArDPD-PO2A** due to the through-space conjugation effect of DPDPO2A. Similarly, in comparison to their analogues, **4ArDPDPO2A** reveal remarkably larger $^1\langle \Psi_H | \Psi_L \rangle$ and smaller $^0d(\Psi_H - \Psi_L)$. It is noteworthy that compared to **4ArPPOPO**, the more centralized FMOs in more twisted **4ArPPODPO** by the steric effect dramatically decrease their $^0\langle \Psi_H | \Psi_L \rangle$ and $^1\langle \Psi_H | \Psi_L \rangle$, and enlarge their $^0d(\Psi_H - \Psi_L)$ and $^1d(\Psi_H - \Psi_L)$, which is the origin of the conflict between ΔE_{ST} and Γ for the insulating D–A–D systems. Obviously, as expected, the employment of homo-conjugated DPDPO2A can realize the best compromise $\langle \Psi_H | \Psi_L \rangle$ through simultaneous ICT enhancement due to the electronic effect and FMO delocalization due to the spatial effect.

In consequence, among these molecules, **4ArDPDPO2A** simultaneously achieve comparable S_1 energy levels, the smallest ΔE_{ST} and the largest $\langle \Psi_H | \Psi_L \rangle$ (Table S2†), which are ascribed to their strongest ICT effects and the uniformly delocalized FMOs, respectively. Therefore, it is convincing that the homoconjugated acceptor-based D–A–D systems would be one of the alternatives with efficient blue TADF emission.

2.3. Optical properties

It is known that the emission color of CT molecules is strongly dependent on the solvent polarity, namely so-called "solvatochromism", which is ascribed to the large polarity difference between their S_0 and S_1 states.[73] Accordingly, the PL spectra of these PO materials are measured in different solvents (Fig. 3a). In high-polarity solvents, the emissions from all the materials are remarkably red-shifted, manifesting their effective ICT interactions. Nevertheless, it is noted that the bathochromic shifts for **4ArDPDPO2A** are the biggest, being 130 nm for the maxima, which is 30 and 40 nm larger than those for **4ArPPOPO** and **4ArPPODPO**, respectively. As a result, along with the increase of solvent polarity (f), the Stokes shift (δ) of
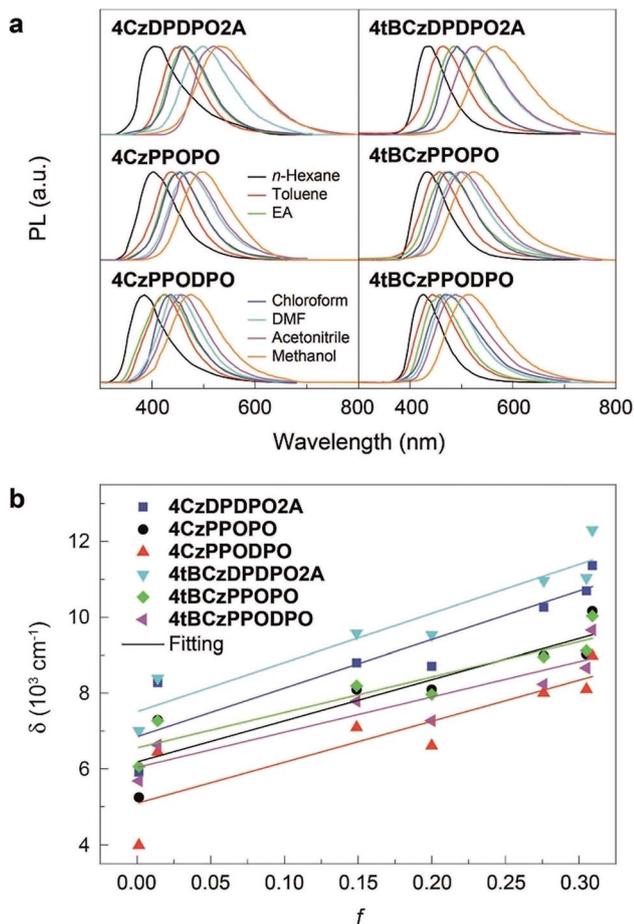
Fig. 3 Solvatochromic properties of **4ArDPDPO2A**, **4ArPPOPO** and **4ArPPODPO**. (a) Spectral variation of **4ArDPDPO2A**, **4ArPPOPO** and **4ArPPODPO** in solvents with different polarities; (b) relationship between solvent orientation polarizability (*f*) and Stokes shift (δ).

4ArDPDPO2A increases more sharply than their analogues, which is quantitatively evidenced by the bigger slopes for the former (Fig. 3b). Consistent with theoretical simulation results, by virtue of the through-space conjugation effect, the ICT intensities in **4ArDPDPO2A** are the strongest among these molecules, whereas the smallest red shifts for **4ArPPODPO** are in accord with their weakest ICT interactions restrained by their twisted configurations. Therefore, with respect to the ICT effect, the linkages in multiple D–A systems are equally important, besides the electronic effects for D and A groups.

The ground-state dipole moment (μ_0) of the molecules is evaluated by DFT calculations (Table S1†). The μ_0 of **4ArDPD-PO2A** is ~4.5–5.1 Debye, which is about 2 Debye smaller than that of **4ArPPOPO** due to the thoroughly symmetrical and coplanar DPDPO2A groups in the former. In the same way, the additional P=O and the twisted configuration provide the biggest μ_0 for **4ArPPODPO**. According to the Lippert–Mataga relationship,[1] the singlet excited-state dipole moment (μ_e) is estimated (Fig. 3b and Table S1†). Because of the reverse order for their ICT intensity, the μ_e differences between **4ArDPDPO2A** and their analogues decrease. Nevertheless, the μ_e of **ArDPDPO2A** which is ~9 Debye is still 1.5–3.5 Debye smaller than that of their

analogues, and even 1.2 and 6.2 Debye smaller than those of their D–A units, respectively, which should be attributed to the uniformly dispersed FMOs on the S_1 states of **ArDPDPO2A**.[66] The small μ_0 of TADF emitters would facilitate their RISC through ΔE_{ST} reduction by the host field effect,[74] while their small μ_e is beneficial to suppress dipole–dipole interaction induced quenching.[22] In this sense, **ArDPDPO2A** would be superior in simultaneous TADF improvement and quenching suppression.

The electronic absorption spectra of all the compounds in dilute chloroform solutions (10^{-6} mol L^{-1}) contain three bands around 230, 285 and 340 nm, corresponding to $\pi \rightarrow \pi^*$ transitions of phenyl and Cz groups and n $\rightarrow$ π^* transitions of the latter, respectively (Fig. 4a and b). More importantly, different from the absorption tails for **4ArPPOPO** and **4ArPPODPO** around 350 nm, **4ArDPDPO2A** reveal additional and distinct CT absorption bands centered at 360 and 375 nm, respectively, further displaying their homoconjugation-enhanced ICT. Meanwhile, all the absorption bands are preserved in the spectra of the neat films, further indicating their limited intermolecular interactions (Fig. S8†). The absorption, fluorescence (FL) and phosphorescence (PH) spectra of these molecules in dilute toluene solutions were further measured to determine their intrinsic excited-state energy levels (Fig. S9†). In accord with TDDFT results, the intramolecular electronic and vibrational couplings facilitate red-shifts of PH spectra for these compounds by 30 nm in comparison to the carbazole molecule. As expected, the red-shifted fluorescence and preserved phosphorescence of **4ArDPDPO2A** give rise to their near-zero ΔE_{ST} of 0.09 and 0.06 eV, respectively, which are remarkably lower by 0.07–0.23 eV in contrast to their nonconjugated analogues (Table S2†).

The vacuum-evaporated films of **4ArDPDPO2A**, **4ArPPOPO** and **4ArPPODPO** as dopants in the 4,6-bis(diphenylphosphoryl) dibenzofuran (**DBFDPO**) matrix were prepared to get an insight into the photophysical properties of the emissive layers (EML) in their OLEDs. The emitters can be homogenously dispersed in **DBFDPO**, resulting in a small Root-Mean-Square roughness around 1 nm (Fig. S11†). All the films reveal blue/sky-blue fluorescence. It is shown that in comparison to Cz-based analogues, the stronger electron-donating effect of the tBCz group results in moderate emission red shifts of ~10 nm (Fig. 4a and b). The FL peak wavelengths of **4ArDPDPO2A** are 470 and 479 nm, respectively, corresponding to sky-blue emissions, which are only 15 and 10 nm larger than those of **4ArP-POPO** and **4ArPPODPO**, respectively. Therefore, as designed, the emission bathochromic shifts of **4ArDPDPO2A** should mainly originate from their enhanced ICT effect rather than the limited conjugation extension by DPDPO2A. The PH spectrum of the **4CzDPDPO2A**-based film at 77 K shows the 0 → 0 transition at 480 nm, giving rise to a small ΔE_{ST} of 0.05 eV, which is only half of ~0.1 eV for its analogues (Table S3†). Therefore, compared to insulating linkages, homoconjugated DPDPO2A can indeed effectively reduce ΔE_{ST}. The PH emission of the **4tBCzDPDPO2A**-based film peaking at 484 nm is almost overlapped with its FL, which further reduces its ΔE_{ST} to 0.03 eV. Nevertheless, **4tBCzPPOPO** and **4tBCzPPODPO** also give ΔE_{ST} as small as 0.04 eV for their films. Since D groups are on both sides of D–A–D systems, D groups with stronger electron-donating
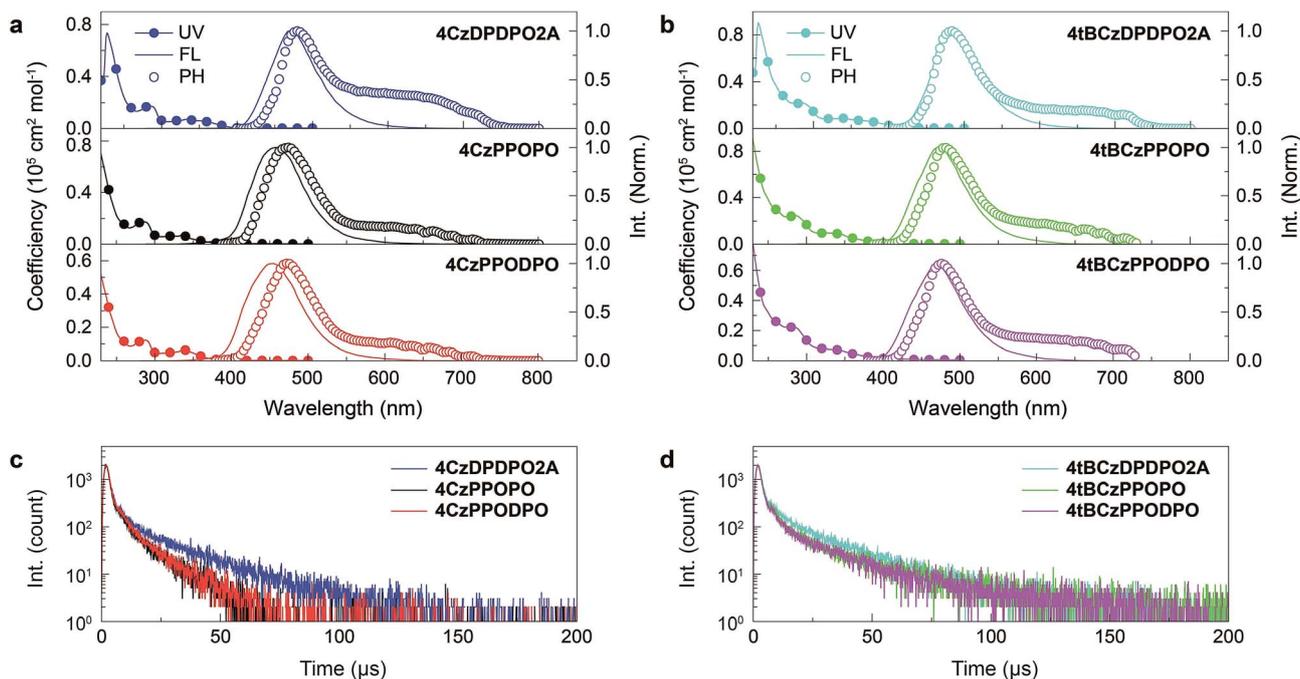
Fig. 4 Photophysical properties of **4ArDPDPO2A**, **4ArPPOPO** and **4ArPPODPO** in the **DBFDPO** matrix. (a) Electronic absorption spectra in dilute CHCl$_3$ (10^{-6} mol L^{-1}), room-temperature fluorescence (FL) and low-temperature time-resolved phosphorescence (PH) spectra in **DBFDPO**-hosted vacuum-evaporated films of **4CzDPDPO2A**, **4CzPPOPO** and **4CzPPODPO** and (b) **4tBCzDPDPO2A**, **4tBCzPPOPO** and **4tBCzPPODPO**; (c) transient emission spectra of **4CzDPDPO2A**, **4CzPPOPO** and **4CzPPODPO** and (d) **4tBCzDPDPO2A**, **4tBCzPPOPO** and **4tBCzPPODPO**.

ability can enhance the local ICT interaction. In this sense, the comparable ΔE_{ST} values of **4CzDPDPO2A**, **4tBCzPPOPO** and **4tBCzPPODPO** actually in turn manifest the effectiveness of through-space conjugation in ICT enhancement. Differently, despite the one more P=O acceptor in **4ArPPODPO**, its ΔE_{ST} is equivalent to that of **4ArPPOPO**, since their insulating linkages restrain D–A interactions in single D–A units rather than entire molecules. Nevertheless, all the molecules reveal typical TADF emissions combined with one short-lifetime PF component (Fig. S10†) and one long-lifetime DF component (Fig. 4c and d).

The rate constants (k) and efficiencies (ϕ) of the key transitions during the TADF process are estimated according to the transient characteristics and ϕ_{PF} and ϕ_{DF} (Fig. 5 and Table S3†).[53] The **4tBCzDPDPO2A**-based film reveals an extremely high k_{PF} at the level of 10^8 s^{-1}, which is among the highest values for blue TADF dyes to date.[56] The k_{PF} of the **4CzDPDPO2A**-based film also reaches 7 × 10^7 s^{-1} which is about half of that of **4tBCzDPDPO2A**, however, it is still 2–3 fold those of **4ArPPOPO** and **4ArPPODPO**. Furthermore, **4ArDPDPO2A** endow their films with an improved k_{DF} of 2–3 × 10^4 s^{-1}, which is 2–4 fold those of **4ArPPOPO** and **4ArPPODPO**. Obviously, the incorporation of the DPDPO2A acceptor in **4ArDPDPO2A** simultaneously facilitates their PF and DF processes, among which **4tBCzDPDPO2A** with stronger D groups is more superior. In this sense, the ICT interaction would be the key influencing factor for the overall photophysical properties of these emitters.

Considering RISC as the core transition for the DF process, the k and ϕ of RISC (k_{RISC} and ϕ_{RISC}) are further evaluated. The k_{RISC} of the **4tBCzDPDPO2A**-based film is beyond 8 × 10^4 s^{-1}, which is 2 fold that of **4CzDPDPO2A** and as high as 8 fold those

of **4ArPPOPO** and **4ArPPODPO**, respectively. At the same time, **4tBCzDPDPO2A** realizes the highest ϕ_{RISC} of 94%, which is beneficial to RISC for overcoming its inferior k in contrast to intersystem crossing (ISC). On the other hand, the rate constants (k_r^S) of singlet radiation for **4ArDPDPO2A**-based films are as high as 2–3 × 10^6 s^{-1}, which is dramatically higher by 4–6 fold in comparison to **4ArPPOPO** and **4ArPPODPO**. Moreover, **4tBCzDPDPO2A** also achieves the lowest rate constant of singlet nonradiation (k_{nr}^S). Nevertheless, the k_{nr}^S values of **4ArDPDPO2A** and **4ArPPODPO** based films are comparable, which are 50% smaller than those of **4ArPPOPO**. The highly rigid coplanar
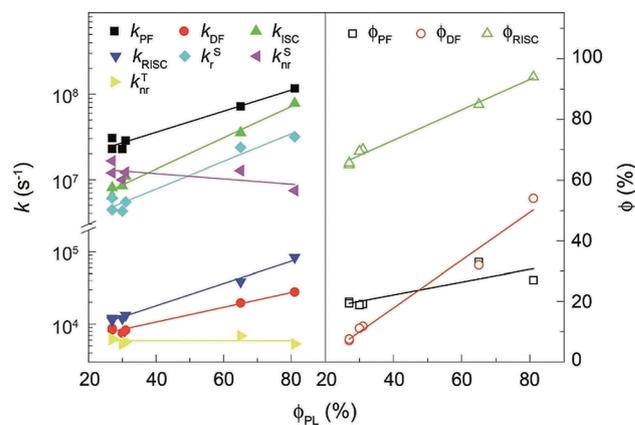

Fig. 5 Linear correlations between ϕ_{PL} of **4ArDPDPO2A**, **4ArPPOPO** and **4ArPPODPO** and the rate constants (k) and efficiencies (ϕ) of the key transitions involved in the TADF process.

structures of **4ArDPDPO2A** and the larger steric hindrance in **4ArPPODPO** with one more *ortho*-DPPO group would restrain the nonradiation paths, *e.g.* excited-state structural relaxation. More significantly, the k_r^Ss of **4ArDPDPO2A** are 2–4 fold larger than their k_{nr}^Ss, but the situation for **4ArPPOPO** and **4ArPPODPO** is just opposite, which indicates the intrinsic superiority of **4ArDPDPO2A** in luminescence. In contrast, the rate constants of triplet nonradiation (k_{nr}^T) for these emitters are nearly equivalent, ascribed to their similar T_1 locations. Nonetheless, with respect to triplet utilization, triplet nonradiation directly competes with RISC. Since the k_{nr}^Ts are more than half of the k_{RISC}s for **4ArPPOPO** and **4ArPPODPO**, but only one seventh or tenth for **4ArDPDPO2A**, the facilitated RISC of **4ArDPDPO2A** actually in turn suppresses triplet nonradiation.

The increased DF emissions from **4ArDPDPO2A**-based films are indicated by their transient emission spectra (Fig. 4c and d). The DF lifetime (τ_{DF}) of **4CzDPDPO2A** reaches 16.2 μs, which is about two fold those of its analogues (Table S3†). The τ_{DF}s of **4tBCzPPOPO** and **4tBCzPPODPO** are comparable to that of **4CzDPDPO2A**, but remarkably shorter than that of **4tBCzDPDPO2A** which is 19.3 μs. The longer τ_{DF} of **4ArDPDPO2A** should be ascribed to the enhanced locally excited feature of their T1 states and the superiority of their rigid cyclic structures in exited-state relaxation suppression. In contrast, the PF lifetimes (τ_{PF}) of **4ArDPDPO2A**-based films are significantly shorter than those of their analogues, which reflects the accelerated singlet radiative transitions for the former. As a consequence, the ϕ_{PL}s of **4ArDPDPO2A** are dramatically improved to 65% and 81%, respectively, which are 2–3 fold those of their analogues. According to the PF and DF ratios in the transient emission spectra, the PF efficiencies (ϕ_{PF}) of **4ArDPDPO2A** are about 30%, which is 50% higher than those of other emitters. More importantly, **4ArDPDPO2A** reveal the state-of-the-art DF efficiencies (ϕ_{DF}) of 32% and 54%, respectively, which are higher by ∼4 fold in contrast to their analogues. Thus, the high ϕ_{PL}s of **4ArDPDPO2A** are mainly contributed by their significantly improved DF emissions, which should be the combined results of their simultaneously facilitated RISC and radiation.

In consequence, **4ArDPDPO2A** successfully demonstrate the feasibility of solving the conflict between ΔE_{ST} and Γ by virtue of the through-conjugation effect of the homoconjugated acceptors, *e.g.* DPDPO2A, which can simultaneously enhance ICT interactions, corresponding to ΔE_{ST} reduction and RISC facilitation, and singlet radiation for efficient TADF emissions. In opposite, it can be noticed that the k and ϕ values of **4ArPPOPO** and **4ArPPODPO** are basically comparable, except for structure-related k_{nr}^S, which is ascribed to the limited intramolecular electronic communications between two D–A units in nonconjugated D–A–D systems. Therefore, the electronic effect is localized by insulating linkage, but uniformized by homoconjugated acceptors, which is the main reason resulting in the dramatically improved photophysical properties of **4ArDPDPO2A**.

2.4. OLED performance

To confirm the superiority of the homoconjugated systems in optoelectronic applications, these molecule doped **DBFDPO**

films were used as EMLs to fabricate OLEDs with a structure of ITO|MoO$_x$ (6 nm)|N,N′-di(1-naphthyl)-N,N′-diphenyl-(1,1′-biphenyl)-4,4′-diamine (**NPB**, 60 nm)|1,3-bis(N-carbazolyl)benzene (**mCP**, 5 nm)|DBFDPO:PO emitters (30 wt%, 30 nm)|**DBFDPO** (45 nm)|LiF (1 nm)|Al (100 nm), in which **NPB** and **mCP** served as hole-transporting and exciton-blocking layers, respectively, and **DBFDPO** was the host matrix and electron-transporting layer (Fig. 6a). The FMO energy levels of the employed materials can be mutually well matched to provide favorable carrier injection. The exciton confinement and carrier capture on the emitters can be further supported by **DBFDPO** with a high T_1 energy level of 3.16 eV and suitable FMO energy levels.[75]

4ArDPDPO2A realize blue and sky-blue electroluminescence (EL) emissions with Commission Internationale de L'Eclairage (CIE) coordinates of (0.17, 0.24) and (0.18, 0.30), respectively (Fig. 6b and Table 1). It is shown that the CIE coordinates of **4CzDPDPO2A**-based devices are comparable to those of **4tBCzPPOPO** and **4tBCzPPODPO**, in accord with their nearly overlapped EL spectra with blue emissions peaking at 460 nm, which are slightly red-shifted in contrast to deep-blue-emitting **4CzPPOPO** and **4CzPPODPO**-based devices with ∼0.05 smaller y coordinates and ∼440 nm EL peaks (inset of Fig. 6c and Table 1). The CIE coordinates of **4tBCzDPDPO2A**-based devices further increase to (0.18, 0.30), accompanied by an EL peak at 472 nm, which corresponds to sky-blue emission. Thus, as designed, the through-space conjugation reveals its superiority in restraining the conjugation-induced bathochromic shift, making homo-conjugated groups "ideal" for constructing blue TADF emitters.

The driving voltages of **4ArDPDPO2A**-based blue devices are the lowest, being about 4, 7 and 10 V at 1, 100 and 1000 nits, which are remarkably lower by 1, 3 and 5 V, respectively, in contrast to their analogues (Fig. 6c and Table 1). On account of the similar current density (J) of these devices, the higher luminance of **4ArDPDPO2A**-based blue devices at the same J should be the main reason for their reduced operating voltages, rather than electrical performance,[21,76] which is further evidenced by their dramatically improved maximum luminance beyond 10^4 nits which is at least 5 fold those for **4ArPPOPO** and **4ArPPODPO** based devices. For the same reason, compared to **4CzDPDPO2A**, **4tBCzDPDPO2A** reduced the driving voltages of its devices by 0.5 V, accompanied by 70% increased maximum luminance.

Inherited from their remarkably higher ϕ_{PL}, **4ArDPDPO2A** significantly elevate EL efficiencies of their blue devices (Fig. 6d and Table 1). The maximum efficiencies of **4tBCzDPDPO2A**-based devices reach 44.8 cd A^{-1} for current efficiency (CE, η_{CE}), 38.0 lm W^{-1} for power efficiency (PE, η_{PE}) and 23.7% for external quantum efficiency (EQE, η_{EQE}), which are favorable for blue TADF diodes reported so far. Considering the outcoupling ratio of ITO glass which is 25%, the exciton utilization efficiency and the internal quantum efficiency of **4tBCzDPDPO2A**-based devices already reached 100%. More importantly, **4tBCzDPDPO2A** reveals the state-of-the-art EL efficiency stability. Its devices realize an η_{EQE} of 22.2 and 18.5% at 100 and 1000 nits, corresponding to EQE roll-offs as low as 6 and 22%, respectively, which is equivalent to the lowest values reported so
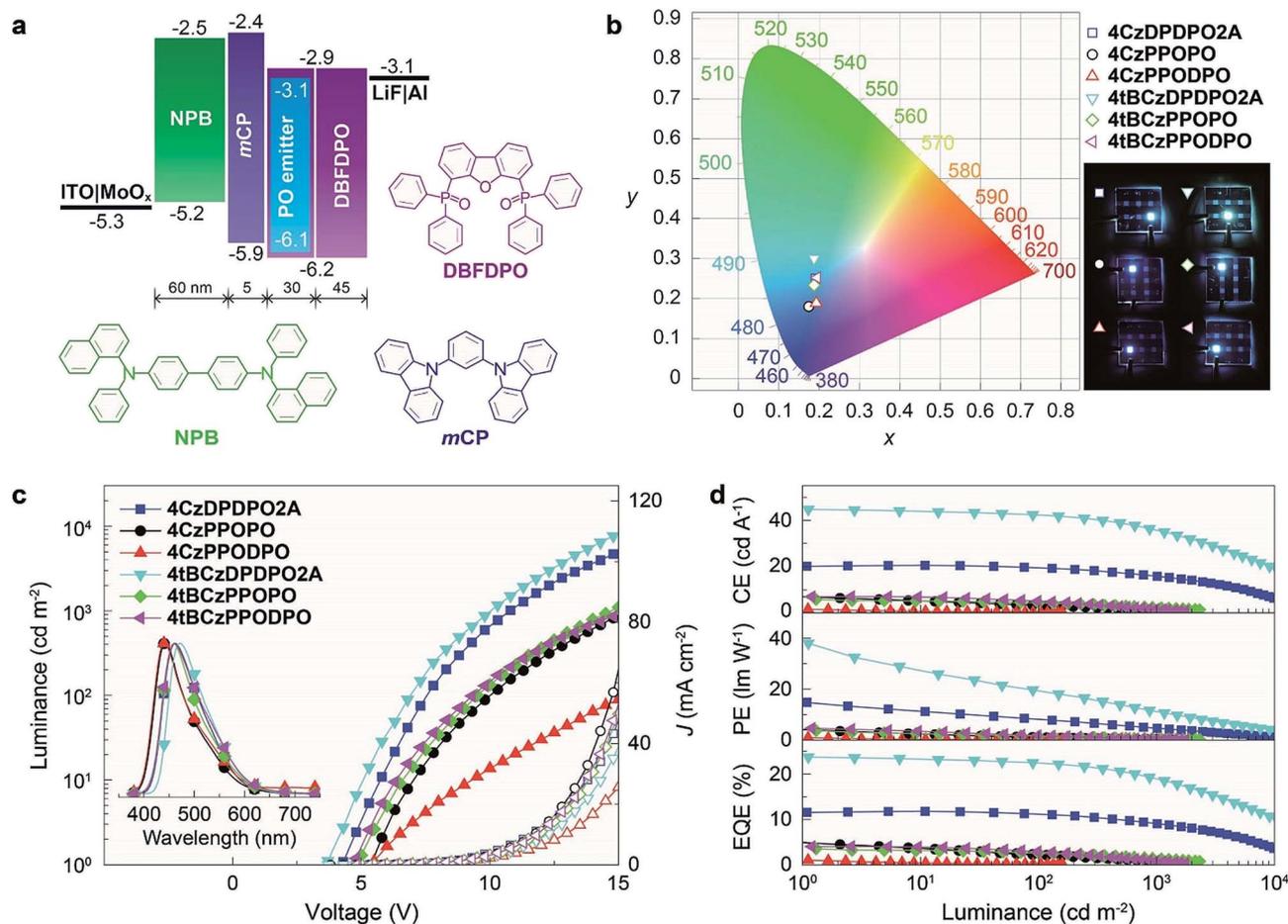
Fig. 6 EL performance of **4ArDPDPO2A**, **4ArPPOPO** and **4ArPPODPO**-based blue OLEDs. (a) Configuration and energetic diagram of the devices and the chemical structures of the employed **DBFDPO** as the host, **NPB** as the hole transporting layer and **mCP** as the exciton-blocking layer; (b) photos and the CIE chromaticity coordinates of the devices; (c) luminance–current density–voltage (L–J–V) characteristics and EL spectra (insets) of the devices; (d) efficiency–luminance relationships of the devices.

far for blue TADF diodes.[77] By contrast, the maximum EL efficiencies of **4CzDPDPO2A**-based blue devices are reduced by about 50%, but its maximum η_{EQE} of 11.5% is still favorable among pure-blue TADF diodes. Especially, most of the pure-blue TADF devices suffer from the serious roll-offs due to the high-energy excitons more sensitive to quenching effects. In contrast, **4CzDPDPO2A** supports its devices with an η_{EQE} of 11.0 and 9.0% at 100 and 1000 nits, corresponding to the impressive EQE roll-offs of 4 and 22%, respectively. In comparison to

4CzDPDPO2A, the maximum EL efficiencies of **4ArPPOPO** and **4ArPPODPO** based devices are further halved, accompanied by sharply worsened roll-offs which are more than 30 and 60% at 100 and 1000 nits, respectively.

It is noteworthy that the maximum η_{EQE}s of these devices reveal a perfect linear dependence on the k and ϕ of the TADF transitions for these emitters, which demonstrates the consistency between photophysical and EL performance modulation (Fig. S12†). Significantly, in comparison to the common focus

Table 1 EL performance of blue OLEDs based on **4ArDPDPO2A**, **4ArPPOPO** and **4ArPPODPO**

Emitter	V^a (V)	L_{max}^b (cd m^{-2})	η_{CE} (cd A^{-1})	η_{PE} (lm W^{-1})	η_{EQE} (%)	λ_{EL}^d/CIE (x, y)
				η^c		
4CzDPDPO2A	4.3, 7.8, 10.8	11 020	20.2, 19.3, 15.9	14.8, 7.8, 4.6	11.5, 11.0, 9.0	460/0.17, 0.24
4CzPPOPO	5.3, 10.3, 15.8	1344	7.1, 3.1, 1.1	4.2, 0.9, 0.2	4.9, 2.1, 0.8	444/0.17, 0.18
4CzPPODPO	5.5, 16.0, —	157	1.6, 0.3, —	0.9, 0.1, —	1.1, 0.2, —	440/0.19, 0.19
4tBCzDPDPO2A	3.7, 7.3, 10.3	18 765	44.8, 41.8, 35.0	38.0, 18.0, 10.7	23.7, 22.2, 18.5	472/0.18, 0.30
4tBCzPPOPO	5.0, 9.5, 15.0	2322	5.8, 4.3, 2.2	3.7, 1.4, 0.5	3.6, 2.6, 1.3	460/0.18, 0.23
4tBCzPPODPO	4.8, 9.3, 16.3	1761	7.0, 5.1, 1.3	4.6, 1.7, 0.2	4.0, 2.9, 0.7	460/0.19, 0.25

^{a} At 1, 100 and 1000 cd m^{-2}. ^{b} The maximum luminance. ^{c} EL efficiencies at the maximum, 100 and 1000 cd m^{-2}. ^{d} EL peak wavelength.

on k_{PF} and k_{DF}, the maximum η_{EQE} is more sensitive to the variations of k_r^S and k_{RISC}, as indicated by the larger slopes of their fitting lines. Therefore, as predicted, the simultaneous enhancement of the singlet radiation and triplet-to-singlet conversion is crucial to improve the EL performance of TADF emitters. Furthermore, in contrast to ϕ_{PF}, the triplet-correlated ϕ_{DF} and ϕ_{RISC} are more influential to the maximum η_{EQE}, which is in accord with the statistical advantage and dominant contribution of triplet excitons for EL. Therefore, it is convincing that the success of **4ArDPDPO2A** in TADF OLEDs originates from the superiority of homoconjugated acceptors in optimizing the photophysical properties of D–A–D systems by the through-space conjugation effect, namely simultaneously enhancing ICT and singlet radiation through FMO optimization.

The excellent EL performance of **4ArDPDPO2A** manifests the great potential of homoconjugated D–A systems as TADF emitters, especially for blue OLEDs. Although the exciton utilization efficiencies (EUE) of **4ArDPDPO2A** approach 100%, the homoconjugated TADF dye still has a huge space for development with respect to D–A combination and optimization.

3. Experimental section

3.1. Fabrication and characterization of OLEDs

Before loading into a deposition chamber, the ITO substrate was cleaned with detergents and deionized water, dried in an oven at 120 °C for 4 h, and treated with oxygen plasma for 3 min. Devices were fabricated by evaporating organic layers at a rate of 0.1–0.2 nm s^{-1} onto the ITO substrate sequentially at a pressure below 4×10^{-4} Pa. Onto the electron-transporting layer, a layer of LiF with 1 nm thickness was deposited at a rate of 0.1 nm s^{-1} to improve electron injection. Finally, a 100 nm-thick layer of Al was deposited at a rate of 0.6 nm s^{-1} as the cathode. The emission area of the devices was 0.09 cm^2 as determined by the overlap area of the anode and the cathode. After fabrication, the devices were immediately transferred to a glove box for encapsulation with glass cover slips using epoxy glue. The EL spectra and CIE coordinates were measured using a PR655 spectra colorimeter. The current–density–voltage and brightness–voltage curves of the devices were measured using a Keithley 4200 source meter and a calibrated silicon photodiode. All the measurements were carried out at room temperature under ambient conditions. For each structure, four devices were fabricated in parallel to confirm the performance repeatability. The device results reported were the data most close to the average values.

4. Conclusions

We demonstrate the feasibility of optimizing the photophysical properties of D–A–D molecules *via* the through-space conjugation effect of homoconjugated acceptors. In contrast to insulating linkage and through-bond conjugation, through-space conjugation provides sufficient intramolecular electronic communication without immoderate conjugated extension. This feature makes it "ideal" for selectively adjusting optoelectronic properties. As evidenced by **4ArDPDPO2A**, besides

preserved blue emissions, the employment of homoconjugated DPDPO2A groups uniformly delocalizes FMOs for simultaneous ICT and $\langle \Psi_H | \Psi_L \rangle$ enhancement, giving rise to their dramatically increased k_{RISC} and k_r^S by 4–6 times. The comprehensively optimized TADF transitions endow **4tBCzDPDPO2A** with ϕ_{PL} and η_{EQE} reaching 81 and 23.7%. This work not only develops a new kind of blue TADF emitter, but also indicates the significance of conjugation optimization for D–A systems, which would accelerate their realistic applications in diverse optoelectronic devices.

Conflicts of interest

There are no conflicts to declare.

Acknowledgements

Notes and references

1 Z. R. Grabowski, K. Rotkiewicz and W. Rettig, *Chem. Rev.*, 2003, **103**, 3899–4032.

2 A. J. Heeger, *Chem. Soc. Rev.*, 2010, **39**, 2354–2371.

3 A. Chaskar, H.-F. Chen and K.-T. Wong, *Adv. Mater.*, 2011, **23**, 3876–3895.

4 D. Yu, F. Zhao, C. Han, H. Xu, J. Li, Z. Zhang, Z. Deng, D. Ma and P. Yan, *Adv. Mater.*, 2012, **24**, 509–514.

5 C. Han, Z. Zhang, H. Xu, J. Li, G. Xie, R. Chen, Y. Zhao and W. Huang, *Angew. Chem., Int. Ed.*, 2012, **51**, 10104–10108.

6 C. Han, Z. Zhang, H. Xu, S. Yue, J. Li, P. Yan, Z. Deng, Y. Zhao, P. Yan and S. Liu, *J. Am. Chem. Soc.*, 2012, **134**, 19179–19188.

7 D. Kim, V. Coropceanu and J.-L. Brédas, *J. Am. Chem. Soc.*, 2011, **133**, 17895–17900.

8 S. Gong, Q. Fu, W. Zeng, C. Zhong, C. Yang, D. Ma and J. Qin, *Chem. Mater.*, 2012, **24**, 3120–3127.

9 Z. Yang, Z. Mao, Z. Xie, Y. Zhang, S. Liu, J. Zhao, J. Xu, Z. Chi and M. P. Aldred, *Chem. Soc. Rev.*, 2017, **46**, 915–1016.

10 H. Uoyama, K. Goushi, K. Shizu, H. Nomura and C. Adachi, *Nature*, 2012, **492**, 234–238.

11 D. M. E. Freeman, A. J. Musser, J. M. Frost, H. L. Stern, A. K. Forster, K. J. Fallon, A. G. Rapidis, F. Cacialli, I. McCulloch, T. M. Clarke, R. H. Friend and H. Bronstein, *J. Am. Chem. Soc.*, 2017, **139**, 11073–11080.

12 G. Xie, X. Li, D. Chen, Z. Wang, X. Cai, D. Chen, Y. Li, K. Liu, Y. Cao and S.-J. Su, *Adv. Mater.*, 2016, **28**, 181–187.

13 Z. Weixuan, L. Hsin-Yu, L. Wei-Kai, J. Min, S. Yi-Jiun, Z. Cheng, G. Shaolong, Z. Tao, X. Guohua, S. Monima, W. Ken-Tsung, W. Chung-Chih and Y. Chuluo, *Adv. Mater.*, 2018, **30**, 1704961.

14 H. Wang, L. Meng, X. Shen, X. Wei, X. Zheng, X. Lv, Y. Yi, Y. Wang and P. Wang, *Adv. Mater.*, 2015, **27**, 4041–4047.

15 Q. Zhang, H. Kuwabara, W. J. Potscavage, S. Huang, Y. Hatae, T. Shibata and C. Adachi, *J. Am. Chem. Soc.*, 2014, **136**, 18070–18081.

16 C. Li, R. Duan, B. Liang, G. Han, S. Wang, K. Ye, Y. Liu, Y. Yi and Y. Wang, *Angew. Chem., Int. Ed.*, 2017, **56**, 11525–11529.

17 L.-S. Cui, Y.-M. Xie, Y.-K. Wang, C. Zhong, Y.-L. Deng, X.-Y. Liu, Z.-Q. Jiang and L.-S. Liao, *Adv. Mater.*, 2015, **27**, 4213–4217.

18 H. G. Kim, K. H. Kim and J. J. Kim, *Adv. Mater.*, 2017, 1702159, DOI: 10.1002/adma.201702159.

19 X.-K. Liu, Z. Chen, C.-J. Zheng, M. Chen, W. Liu, X.-H. Zhang and C.-S. Lee, *Adv. Mater.*, 2015, **27**, 2025–2030.

20 D. Zhang, X. Song, M. Cai and L. Duan, *Adv. Mater.*, 2018, **30**, 1705250.

21 J. Zhang, D. Ding, Y. Wei, F. Han, H. Xu and W. Huang, *Adv. Mater.*, 2016, **28**, 479–485.

22 C. Han, Z. Zhang, D. Ding and H. Xu, *Chem*, 2018, **4**, 2154–2167.

23 Y. Tao, L. Xu, Z. Zhang, R. Chen, H. Li, H. Xu, C. Zheng and W. Huang, *J. Am. Chem. Soc.*, 2016, **138**, 9655–9662.

24 C. Han, C. Duan, W. Yang, M. Xie and H. Xu, *Sci. Adv.*, 2017, **3**, e1700904.

25 H. Liu, Q. Bai, L. Yao, H. Zhang, H. Xu, S. Zhang, W. Li, Y. Gao, J. Li, P. Lu, H. Wang, B. Yang and Y. Ma, *Chem. Sci.*, 2015, **6**, 3797–3804.

26 W.-Y. Wong and C.-L. Ho, *Acc. Chem. Res.*, 2010, **43**, 1246–1256.

27 S. Dai, T. Li, W. Wang, Y. Xiao, T. K. Lau, Z. Li, K. Liu, X. Lu and X. Zhan, *Adv. Mater.*, 2018, **30**, 1706571.

28 J. D. Chen, Y. Q. Li, J. Zhu, Q. Zhang, R. P. Xu, C. Li, Y. X. Zhang, J. S. Huang, X. Zhan, W. You and J. X. Tang, *Adv. Mater.*, 2018, **30**, 1706083.

29 S. Mathew, A. Yella, P. Gao, R. Humphry-Baker, F. E. CurchodBasile, N. Ashari-Astani, I. Tavernelli, U. Rothlisberger, K. NazeeruddinMd and M. Grätzel, *Nat. Chem.*, 2014, **6**, 242–247.

30 Z. He, C. Zhong, S. Su, M. Xu, H. Wu and Y. Cao, *Nat. Photonics*, 2012, **6**, 593–597.

31 Q. Zhang, B. Kan, F. Liu, G. Long, X. Wan, X. Chen, Y. Zuo, W. Ni, H. Zhang, M. Li, Z. Hu, F. Huang, Y. Cao, Z. Liang, M. Zhang, T. P. Russell and Y. Chen, *Nat. Photonics*, 2015, **9**, 35–41.

32 Y. Sun, G. C. Welch, W. L. Leong, C. J. Takacs, G. C. Bazan and A. J. Heeger, *Nat. Mater.*, 2012, **11**, 44–48.

33 M. Qian, R. Zhang, J. Hao, W. Zhang, Q. Zhang, J. Wang, Y. Tao, S. Chen, J. Fang and W. Huang, *Adv. Mater.*, 2015, **27**, 3546–3552.

34 H. Zhang, Y. Wu, W. Zhang, E. Li, C. Shen, H. Jiang, H. Tian and W.-H. Zhu, *Chem. Sci.*, 2018, **9**, 5919–5928.

35 H. Dong, H. Zhu, Q. Meng, X. Gong and W. Hu, *Chem. Soc. Rev.*, 2012, **41**, 1754–1808.

36 K.-J. Baeg, M. Binda, D. Natali, M. Caironi and Y.-Y. Noh, *Adv. Mater.*, 2013, **25**, 4267–4295.

37 R. H. Kim, H. J. Kim, I. Bae, S. K. Hwang, D. B. Velusamy, S. M. Cho, K. Takaishi, T. Muto, D. Hashizume, M. Uchiyama, P. André, F. Mathevet, B. Heinrich, T. Aoyama, D.-E. Kim, H. Lee, J.-C. Ribierre and C. Park, *Nat. Commun.*, 2014, **5**, 3583.

38 T. Sekitani, T. Yokota, U. Zschieschang, H. Klauk, S. Bauer, K. Takeuchi, M. Takamiya, T. Sakurai and T. Someya, *Science*, 2009, **326**, 1516–1519.

39 V. K.-M. Au, D. Wu and V. W.-W. Yam, *J. Am. Chem. Soc.*, 2015, **137**, 4654–4657.

40 R. Kabe and C. Adachi, *Nature*, 2017, **550**, 384–387.

41 X. Xiong, F. Song, J. Wang, Y. Zhang, Y. Xue, L. Sun, N. Jiang, P. Gao, L. Tian and X. Peng, *J. Am. Chem. Soc.*, 2014, **136**, 9590–9597.

42 Z. He, W. Zhao, J. W. Y. Lam, Q. Peng, H. Ma, G. Liang, Z. Shuai and B. Z. Tang, *Nat. Commun.*, 2017, **8**, 416.

43 Z. An, C. Zheng, Y. Tao, R. Chen, H. Shi, T. Chen, Z. Wang, H. Li, R. Deng, X. Liu and W. Huang, *Nat. Mater.*, 2015, **14**, 685–690.

44 H. N. Kim, Z. Guo, W. Zhu, J. Yoon and H. Tian, *Chem. Soc. Rev.*, 2011, **40**, 79–93.

45 X. Guo, M. Zhang, J. Tan, S. Zhang, L. Huo, W. Hu, Y. Li and J. Hou, *Adv. Mater.*, 2012, **24**, 6536–6541.

46 H. Meier, *Angew. Chem., Int. Ed.*, 2005, **44**, 2482–2506.

47 M. W. Wolf, K. D. Legg, R. E. Brown, L. A. Singer and J. H. Parks, *J. Am. Chem. Soc.*, 1975, **97**, 4490–4497.

48 J. Partee, E. L. Frankevich, B. Uhlhorn, J. Shinar, Y. Ding and T. J. Barton, *Phys. Rev. Lett.*, 1998, **82**, 3673–3676.

49 A. Endo, M. Ogasawara, A. Takahashi, D. Yokoyama, Y. Kato and C. Adachi, *Adv. Mater.*, 2009, **21**, 4802–4806.

50 G. X. Yifan Li, S. Gong, K. Wu and C. Yang, *Chem. Sci.*, 2016, **7**, 5441–5447.

51 X. Cai, X. Li, G. Xie, Z. He, K. Gao, K. Liu, D. Chen, Y. Cao and S.-J. Su, *Chem. Sci.*, 2016, **7**, 4264–4275.

52 M. Klessinger, *Angew. Chem., Int. Ed.*, 1995, **34**, 549–551.

53 Y. Tao, K. Yuan, T. Chen, P. Xu, H. Li, R. Chen, C. Zheng, L. Zhang and W. Huang, *Adv. Mater.*, 2014, **26**, 7931–7958.

54 E. Fermi, *Nuclear Physics: A Course Given by Enrico Fermi at the University of Chicago*, University of Chicago Press, Chicago, 1950.

55 T. J. Penfold, F. B. Dias and A. P. Monkman, *Chem. Commun.*, 2018, **54**, 3926–3935.

56 S. Hirata, Y. Sakai, K. Masui, H. Tanaka, S. Y. Lee, H. Nomura, N. Nakamura, M. Yasumatsu, H. Nakanotani, Q. Zhang, K. Shizu, H. Miyazaki and C. Adachi, *Nat. Mater.*, 2015, **14**, 330–336.

57 Q. Zhang, J. Li, K. Shizu, S. Huang, S. Hirata, H. Miyazaki and C. Adachi, *J. Am. Chem. Soc.*, 2012, **134**, 14706–14709.

58 Q. Zhang, B. Li, S. Huang, H. Nomura, H. Tanaka and C. Adachi, *Nat. Photonics*, 2014, **8**, 326–332.

59 P. Rajamalli, N. Senthilkumar, P. Gandeepan, P.-Y. Huang, M.-J. Huang, C.-Z. Ren-Wu, C.-Y. Yang, M.-J. Chiu, L.-K. Chu, H.-W. Lin and C.-H. Cheng, *J. Am. Chem. Soc.*, 2016, **138**, 628–634.

60 P. Rajamalli, N. Senthilkumar, P. Y. Huang, C. C. Ren-Wu, H. W. Lin and C. H. Cheng, *J. Am. Chem. Soc.*, 2017, **139**, 10948–10951.

61 Y. J. Cho, S. K. Jeon, B. D. Chin, E. Yu and J. Y. Lee, *Angew. Chem., Int. Ed.*, 2015, **54**, 5201–5204.

62 C. Duan, J. Li, C. Han, D. Ding, H. Yang, Y. Wei and H. Xu, *Chem. Mater.*, 2016, **28**, 5667–5679.

63 C. Li, C. Duan, C. Han and H. Xu, *Adv. Mater.*, 2018, **30**, 1804228.

64 J. F. Coetzee and G. R. Padmanabhan, *J. Phys. Chem.*, 1965, **69**, 3193–3196.

65 K. Kawasumi, T. Wu, T. Zhu, H. S. Chae, T. Van Voorhis, M. A. Baldo and T. M. Swager, *J. Am. Chem. Soc.*, 2015, **137**, 11908–11911.

66 Q. Liang, C. Han, C. Duan and H. Xu, *Adv. Magn. Opt. Mater.*, 2018, **6**, 1800020.

67 L. T. Scott, *Pure Appl. Chem.*, 1986, **58**, 105–110.

68 J. Li, D. Ding, Y. Wei, J. Zhang and H. Xu, *Adv. Magn. Opt. Mater.*, 2016, **4**, 522–528.

69 Y. Pan, W. Li, S. Zhang, L. Yao, C. Gu, H. Xu, B. Yang and Y. Ma, *Adv. Magn. Opt. Mater.*, 2014, **2**, 510–515.

70 T. Chen, L. Zheng, J. Yuan, Z. An, R. Chen, Y. Tao, H. Li, X. Xie and W. Huang, *Sci. Rep.*, 2015, **5**, 10923.

71 J. Gibson, A. P. Monkman and T. J. Penfold, *ChemPhysChem*, 2016, **17**, 2956–2961.

72 S. Manzetti and T. Lu, *J. Phys. Org. Chem.*, 2013, **26**, 473–483.

73 R. Ishimatsu, S. Matsunami, K. Shizu, C. Adachi, K. Nakano and T. Imato, *J. Phys. Chem. A*, 2013, **117**, 5607–5612.

74 G. Méhes, K. Goushi, W. J. Potscavage Jr and C. Adachi, *Org. Electron.*, 2014, **15**, 2027–2037.

75 C. Han, G. Xie, J. Li, Z. Zhang, H. Xu, Z. Deng, Y. Zhao, P. Yan and S. Liu, *Chem.–Eur. J.*, 2011, **17**, 8947–8956.

76 Z. Zhang, Z. Zhang, D. Ding, Y. Wei, H. Xu, J. Jia, Y. Zhao, K. Pan and W. Huang, *J. Phys. Chem. C*, 2014, **118**, 20559–20570.

77 H. Yang, Q. Liang, C. Han, J. Zhang and H. Xu, *Adv. Mater.*, 2017, **29**, 1700553.